Received: 27 February 2024 | Revised: 29 August 2024 | Accepted: 5 September 2024

DOI: 10.1002/mp.17427

RESEARCH ARTICLE

MEDICAL PHYSICS

Transducer module apodization to reduce bone heating during focused ultrasound uterine fibroid ablation with phased arrays: A numerical study

Sobhan Goudarzi[1] | **Ryan Matthew Jones**[1] | **Yin Hau Wallace Lee**[1] | **Kullervo Hynynen**[1,2,3]

[1]Physical Sciences Platform, Sunnybrook Research Institute, Toronto, Ontario, Canada

[2]Department of Medical Biophysics, University of Toronto, Toronto, Ontario, Canada

[3]Institute of Biomedical Engineering, University of Toronto, Toronto, Ontario, Canada

Correspondence
Sobhan Goudarzi, Sunnybrook Research Institute, Toronto, Ontario M4N 3M5, Canada.
Email: sobhan.goudarzi@sri.utoronto.ca

Funding information
Strategic Innovation Fund, Grant/Award Number: 2020-1014; Ontario Research Foundation, Grant/Award Number: RE08020; Arrayus Technologies

Abstract

Background: During magnetic resonance-guided focused ultrasound (MRgFUS) surgery for uterine fibroids, ablation of fibrous tissues in proximity to the hips and spine is challenging due to heating within the bone that can cause patients to experience pain and potentially damage nerves. This far-field bone heating limits the volume of fibroid tissue that is treatable via MRgFUS.

Purpose: To investigate transducer module apodization for improving the ratio of focal-to-bone heating (ΔT_{ratio}) when targeting fibroid tissue close to the hips and spine, to enable MRgFUS treatments closer to the bone.

Methods: Acoustic and thermal simulations were performed using 3D magnetic resonance imaging (MRI)-derived anatomies of ten patients who underwent MRgFUS ablation for uterine fibroids using a low-frequency (0.5 MHz) 6144-element flat fully-populated modular phased array system (Arrayus Technologies Inc., Burlington, Canada) at our institution as part of a larger clinical trial (NCT03323905). Transducer modules (64 elements per module) whose beams intersected with no-pass zones delineated within the field were identified, their output power levels were reduced by varying blocking percentage levels, and the resulting temperature field distributions were evaluated across multiple sonications near the hip and spine bones in each patient. Acoustic and thermal simulations took approximately 20 min (7 min) and 1 min (30 s) to run for a single near-spine (near-hip) target, respectively.

Results: For all simulated sonications, transducer module blocking improved ΔT_{ratio} compared to the no blocking case. In just over half of sonications, full module blocking maximized ΔT_{ratio} (increase of 82% ± 38% in 50% of hip targets and 49% ± 30% in 62% of spine targets vs. no blocking; mean ± SD), at the cost of more diffuse focusing (focal heating volumes increased by 13% ± 13% for hip targets and 39% ± 27% for spine targets) and thus requiring elevated total (hip: 6% ± 17%, spine: 37% ± 17%) and peak module-wise (hip: 65% ± 36%, spine: 101% ± 56%) acoustic power levels to achieve equivalent focal heating as the no blocking control case. In the remaining sonications, partial module blocking provided further improvements in both ΔT_{ratio} (increased by 29% ± 25% in the hip and 15% ± 12% in the spine) and focal heating volume (decrease of 20% ± 10% in the hip and 34% ± 17% in the spine) relative to the full blocking case. The optimal blocking percentage value was dependent on the specific patient geometry and target location of interest. Although not all individual target locations saw the benefit, element-wise phase aberration corrections improved the average ΔT_{ratio} compared to the no correction case (increase of 52% ± 47% in the hip, 35% ± 24%

in the spine) and impacted the optimal blocking percentage value. Transducer module blocking enabled ablative treatments to be carried out closer to both hip and spine without overheating or damaging the bone (no blocking: 42 ± 1 mm/17 ± 2 mm, full blocking: 38 ± 1 mm/8 ± 1 mm, optimal partial blocking: 36 ± 1 mm/7 ± 1 mm for hip/spine).
Conclusion: The proposed transducer apodization scheme shows promise for improving MRgFUS treatments of uterine fibroids, and may ultimately increase the effective treatment envelope of MRgFUS surgery in the body by enabling tissue ablation closer to bony structures.

KEYWORDS
image guided therapy, MRgFUS, numerical simulations, phased arrays, treatment planning, uterine fibroids

1 | INTRODUCTION

Uterine fibroids,[1] also known as myomas or leiomyomas, are benign tumors or neoplasms of the uterus that account for substantial health care costs worldwide (e.g., estimated total cost of $5.9–$34.4 billion annually in the United States of America[2]). Fibroids are common and have been reported to occur in over 70% of females, with clinical symptoms reported in 25%–50% of women, and can cause symptoms so debilitating that surgical removal of the tumor(s) is necessary. Existing treatment options for symptomatic fibroids include invasive surgical procedures (e.g., hysterectomies or myomectomies), hormone-based medical treatment, as well as minimally invasive and noninvasive techniques for women who wish to preserve their fertility (e.g., uterine artery embolization or focused ultrasound (FUS) surgery). FUS surgery, which can be performed under ultrasound[3] or magnetic resonance (MR)[4] imaging guidance, is a noninvasive ablative therapy that harnesses acoustic energy directed through the abdominal wall to elevate local temperatures and induce thermal coagulative necrosis within targeted fibroid regions, while leaving surrounding tissue(s) unaffected. MR-guided FUS (MRgFUS) procedures provide superior image guidance, allowing for precise targeting, online monitoring via MR-thermography, and posttreatment evaluation of the ultrasound-mediated bioeffects.[5]

Existing commercial MRgFUS devices for the treatment of uterine fibroids include single-element transducers[6] as well as multielement phased array systems.[4,7,8] Phased arrays offer several advantages for MRgFUS therapy compared to single-element transducers, including the ability to rapidly scan the focal spot, compensate for beam aberrations, and tailor the acoustic energy distribution for a given therapeutic application.[9] Both the ExAblate Body (InSightec Inc., Tirat Carmel, Israel)[4] and Sonalleve (Profound Medical Inc., Mississauga, Canada)[8] MRgFUS devices operate at frequencies near 1 MHz and employ spherically-curved phased arrays with relatively large array elements. The use of large elements combined with spherically-focused apertures results in limited electronic steering capabilities, such that mechanical translation and/or rotation of the transducer is required to perform large volume treatments with these applicators. A more recently developed MRgFUS device (Arrayus Technologies Inc., Burlington, Canada) operates at a lower frequency of 0.5 MHz[10–12] and consists of a flat fully-populated modular phased array that is designed for large volume tissue ablation without the need for mechanical repositioning of the transducer.[7] Promising clinical results have been obtained treating women with uterine fibroids with these MRgFUS systems.[7,13–16]

Because bone has a much higher propensity to absorb acoustic energy than soft-tissues, under certain conditions substantial temperature elevations can be generated at bone interfaces.[17–21] A rare complication that has been documented following FUS treatments of uterine fibroids is damage to nerves located near regions of bone heating beyond the focal point (e.g., hips with lateral targets, spine with deep targets).[13,22] Since temperature-induced pain thresholds are considerably lower than those for irreversible thermal damage, clinically-approved fibroid systems provide patients with a button to stop sonications with the onset of pain to protect against such far-field damage. Although this is encouraging from a safety perspective, these far-field bone heating effects ultimately limit the volume of fibroid tissue that is treatable via MRgFUS. Efforts to minimize unwanted bone heating with high-frequency spherically-curved phased arrays include ensuring a sufficient stand-off distance between the fibroid target and the closest bone surface (e.g., 4 cm for the ExAblate Body[22] and Sonalleve[23] devices), mechanical tilting of the MRgFUS transducer to minimize the beam's interaction with bone in the far field, and rectal filling to displace the fibroid from the bone.[24] These unwanted heating effects can be further pronounced with lower operating frequencies, since more energy is deposited in the far

field, such that larger bone stand-off distances may be required.[7,11]

A major benefit of phased array transducers is their ability to tailor the beam geometry and direction electronically to provide optimal energy deposition patterns for specific treatment scenarios.[9] Indeed, the capability of performing electronic beam shaping to minimize acoustic energy deposition within sensitive tissue regions has been integrated into several clinical MRgFUS phased array systems.[25–27] In its most basic form, beam shaping can be accomplished by deactivating individual transducer elements that contribute to acoustic deposition within no-pass zones in the field delineated in software by the MRgFUS system operator. In the context of MRgFUS treatments of uterine fibroids, these no-pass zones commonly include scar tissue or bowel regions within the near-field.[25,26] Electronic beam shaping has also been investigated for reducing near-field temperature elevations within bone during preclinical MRgFUS treatments, including trans-costal applications (e.g., liver treatments) to minimize rib heating.[28–33] Similar approaches may help minimize far-field bone heating in the hips and spine during uterine fibroid treatments.

In this study, we investigate phased array transducer apodization strategies in silico for reducing far-field bone heating during trans-abdominal MRgFUS. Acoustic and thermal simulations were performed using MRI-derived anatomies of ten patients who underwent MRgFUS ablation for uterine fibroids using a low-frequency flat fully-populated modular phased array system. Array elements within transducer modules whose beams intersected with no-pass zones were identified, their output power levels were reduced by varying blocking percentage levels, and the resulting temperature field distributions were evaluated across multiple simulated sonications with varying stand-off distances from hip and spine bones. Simulations were carried out both with and without phase aberration corrections incorporated in the array element driving signals to compensate for soft-tissue field distortions. Optimal blocking percentage levels, defined as the value that maximized the focal-to-bone heating ratio, were identified for each sonication. Finally, we estimate how close to bone ablative sonications may be feasible using this MRgFUS device with various blocking percentage levels.

2 | METHODS

2.1 | Transducer design

The ultrasound device simulated in this study is a flat fully-populated modular MRgFUS phased array system designed for abdominal applications (Arrayus Technologies Inc., Burlington, Canada). The phased array consists of square 1.35 mm × 1.35 mm transducer elements grouped into 8 × 8 square modules[7,12,34] with a half-wavelength (1.5 mm) inter-element spacing at the driving frequency (frequency = 518 kHz, lateral vibration mode[35]). The patients investigated in this study were treated using a 170 mm-diameter, 6144-element (96-module) array constructed in-house (Figure 1a). The transducer array's design is based on prior simulation work that investigated large-aperture, flat, densely-populated phased arrays and their ability to treat large tissue volumes to complete fibroid patient treatments without needing to reposition the device.[10–12] At a target depth of 60 mm, the on-axis focal beam width and depth of field (intensity full-width at half-maxima) of this device were assessed via hydrophone measurements (HNP-0400, Onda Corporation, Sunnyvale, CA, USA) to be 1.9 mm and 7.0 mm, respectively, consistent with numerical simulations.[10] The phased array is housed in a reservoir that nominally extends 5 mm in front of its active surface within which chilled degassed water is circulated to cool the transducer head. A degassed water pad, with diluted/degassed ultrasound gel on top, provides acoustic coupling between the reservoir and the patient (Figure 1b).

2.2 | Anatomical model

MRI datasets from ten patients who underwent MRgFUS for the treatment of uterine fibroids at Sunnybrook Research Institute (Toronto, ON, Canada) between December 2019 and August 2021 as part of a larger clinical trial (NCT03323905) were anonymized for use within this study. Pretreatment sagittal T2-weighted (3D SPACE turbo spin echo; repetition time: 2000 ms, echo time: 81 ms, slice thickness: 2 mm) abdominal scans acquired on a 3T MRI scanner (MAGNETOM Prisma, Siemens Healthcare, Erlangen, Germany) were segmented manually to delineate boundaries between the acoustic coupling pad, skin, fat, muscle, fibroid, bowel, spine, and hip regions, as illustrated in (Figure 1b). Because poor MR image quality close to the ultrasound transducer array precluded accurate skin layer segmentation, this layer was generated synthetically in each patient with a constant 2 mm offset distance from the corresponding fat-muscle layer. Foley catheters located within the bladder region were segmented when present. Tissue boundaries were exported in XML format using the MIPAV software suite,[55] and triangulated meshes of the various tissue boundary layers were generated using the *isosurface* function in MATLAB (R2018b, Mathworks, Natick, MA). All tissue layer meshes were created with element surface areas less than or equal to $(\lambda/6)^2$, where λ is the acoustic wavelength in water. The resulting meshes were smoothed[56] to mitigate discontinuities arising from the manual segmentation process. The sound speed values assigned to the chilled water

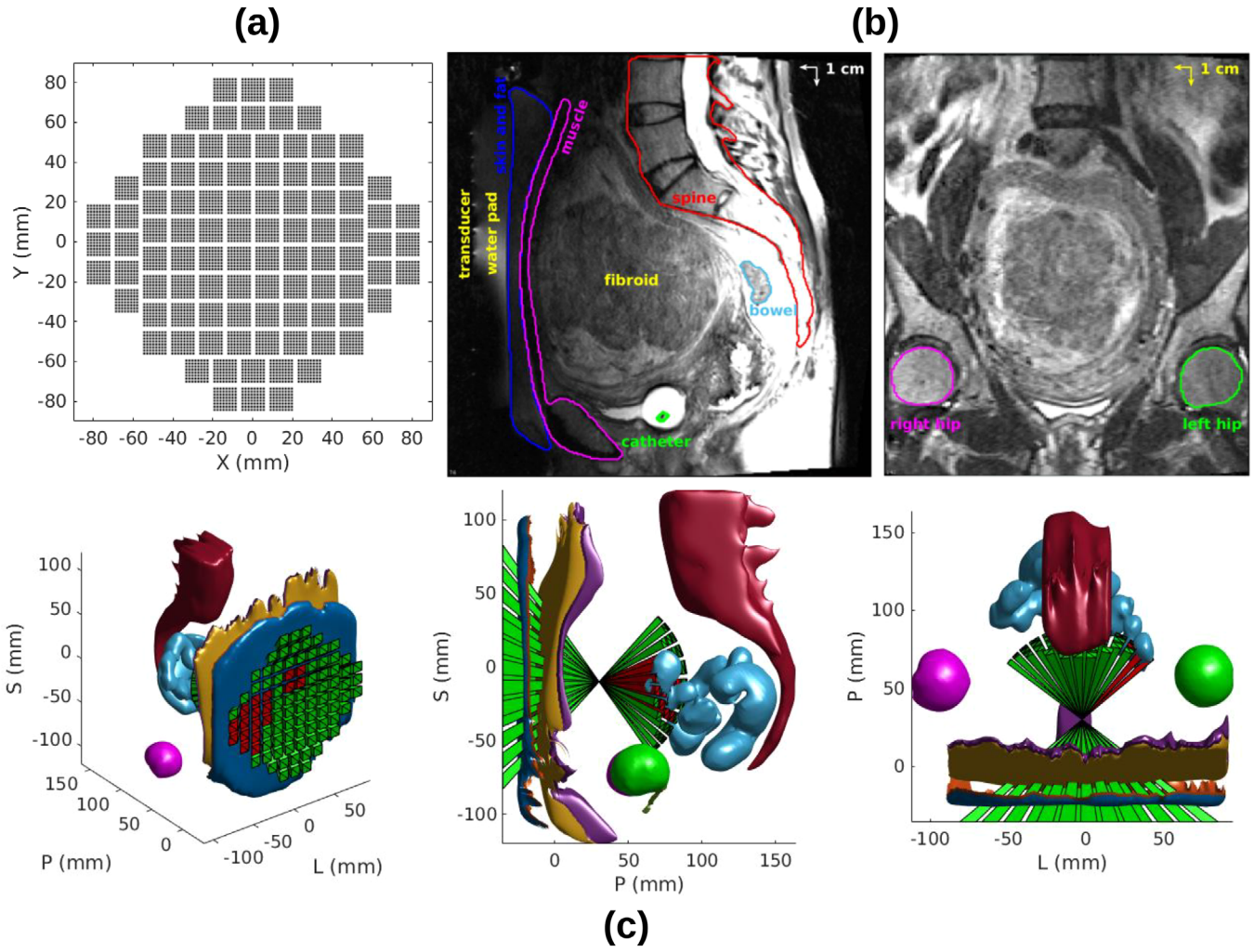

FIGURE 1 (a) Top-down view of the phased array, which comprises 96 square-shaped 64-element modules (6144 elements total). (b) Example sagittal (left) and coronal (right) T2-weighted MR images from patient #1, illustrating contoured tissue regions. (c) 3D simulation model generated from segmentation masks across all MRI slices, with different tissue layers colour-coded (consistent with colours in [b]). Transducer module beam visualisation for an example sonication is shown to illustrate the module blocking algorithm; modules whose beams intersect with the no-pass bowel region (cyan) are shown in red, whereas nonintersecting modules are shown in green. L = left, P = posterior, S = superior.

reservoir (10 °C, sound speed = 1447 m/s) and water pad (24 °C, sound speed = 1492 m/s) regions were temperature-dependent.[41] The 3D model domain for a representative patient is illustrated in (Figure 1c). The acoustic and thermal parameters of different media in our simulation model are provided in Table 1.

2.3 | Simulation model

A multilayered ray acoustics model was used to simulate trans-abdominal ultrasound propagation. In this model, developed originally by Fan and Hynynen,[57,58] transmission and reflection at boundaries separating two media with different acoustical properties are approximated using the boundary conditions for plane waves obliquely incident upon a planar interface. Shear mode conversion was incorporated at fluid-solid (i.e., soft tissue-bone) interfaces,[59–61] resulting in the propagation of both longitudinal and shear wave components within the bone. Pennes' bioheat transfer equation was employed to model ultrasound-induced heating effects at the focus and in near-bone regions.[62] These models have been validated in multiple studies comparing simulated predictions to experimental measurements.[12,58,63–65]

2.3.1 | Acoustic model

Starting at the transducer surface, longitudinal particle velocities were propagated from a source layer to a

TABLE 1 Acoustic and thermal parameters employed in silico for different media.

Parameter \ Medium	Water pad	Skin	Fat	Muscle	Fibroid	Bowel	Spine	Hip	Blood
Density (ρ, kg/m^3)	1000[36]	1200[37]	921[38]	1138[38]	1052[38]	1.1[11]	1850[39]	1850[39]	1050[40]
Longitudinal Sound Speed (c_L, m/s)	1492[41]	1645[42]	1445[38]	1569[38]	1614[38]	353[11]	3500[43]	2941[43]	1590[43]
Shear Sound Speed (c_S, m/s)	N/A	N/A	N/A	N/A	N/A	N/A	1400[44]	1760[43]	N/A
Longitudinal Attenuation (α_L, Np/m/MHz)	0	40[43]	7[45]	4.1[45]	8.6[43]	N/A	124.5[46]	79.4[43]	N/A
Shear Attenuation (α_S, Np/m/MHz)	N/A	N/A	N/A	N/A	N/A	N/A	90[44]	115.1[47]	N/A
Specific Heat Capacity (C, J/kg/^{o}C)	4180[36]	3410[48]	2490[36]	3565[43]	3434[49]	N/A	1300[43]	1300[43]	3850[50]
Thermal Conductivity (κ, W/m/K)	0.615[36]	0.376[37]	0.248[43]	0.498[43]	0.5[49]	N/A	0.36[43]	0.36[43]	0.506[51]
Perfusion Rate (ω, 1/s)	0	5.83×10^{-452}	5×10^{-436}	3.97×10^{-453}	1.8×10^{-354}	N/A	3.33×10^{-446}	3.33×10^{-446}	N/A

Note: Shear waves were only modeled in bone tissues (i.e., spine and hip).

target layer as follows:[58]

$$u_n(\mathbf{r}') = \frac{jk}{2\pi}\int_S u_n(\mathbf{r})\frac{e^{-jk||\mathbf{r}'-\mathbf{r}||}}{||\mathbf{r}'-\mathbf{r}||}\left(1-\frac{j}{k||\mathbf{r}'-\mathbf{r}||}\right) T\cos(\theta)ds, \quad (1)$$

where k is the complex wavenumber ($k = 2\pi f/c - j\alpha$, with f the driving frequency, c the sound speed, and α the attenuation coefficient), $u_n(\mathbf{r})$ is the normal component of the particle velocity of the source sub-element located at $\mathbf{r}$ with surface area ds, S is the source surface over which the integration is carried out, and $||\mathbf{r}'-\mathbf{r}||$ is the Cartesian distance between the target layer sub-element at $\mathbf{r}'$ and the source sub-element at $\mathbf{r}$. T and θ represent the particle velocity transmission coefficient and transmission angle at the interface, respectively, the latter of which is dictated by Snell's law. Reflected particle velocities are computed on layer surfaces in a similar fashion, but with T replaced by the particle velocity reflection coefficient and θ replaced by the reflection angle. Particle velocity transmission and reflection coefficients at both fluid-fluid[58] and fluid-solid[44,66,67] interfaces are well documented in the literature.

Once the particle velocities on the muscle-fibroid boundary layer (Figure 1b) were obtained, and pressure fields surrounding the focal point and in near-bone regions were computed using the Rayleigh integral, two forms of which were applied in this study. The acoustic pressure at any point within the region of interest ($\mathbf{r}$) was calculated via:[57]

$$p(\mathbf{r}') = \frac{jk\rho c}{2\pi}\int_S u_n(\mathbf{r})\frac{e^{-jk||\mathbf{r}'-\mathbf{r}||}}{||\mathbf{r}'-\mathbf{r}||}ds, \quad (2)$$

where ρ denotes the density of the propagation medium. Reflections from both bowel and bone surfaces were considered when computing pressure fields in soft-tissue within the focal and near-bone regions. In some patients, portions of the spine were obscured by intervening bowel volumes. Within bone, pressure contributions from both the longitudinal and shear wave components were calculated independently. For points very close to the source layer boundary, the pressure field was calculated via:[68]

$$p(\mathbf{r}') = \frac{jk\rho c}{2\pi}\int_{S_0} u_n(\mathbf{r})\frac{e^{-jk||\mathbf{r}'-\mathbf{r}||}}{||\mathbf{r}'-\mathbf{r}||}\,ds - \rho c u_n(\mathbf{r})[e^{-jk\epsilon}-1]\Big|_{S_\epsilon}, \quad (3)$$

where the surface S is divided into S_0 for all $||\mathbf{r}'-\mathbf{r}|| > \epsilon$ and S_ϵ for all $||\mathbf{r}'-\mathbf{r}|| \le \epsilon$, with $\epsilon = \sqrt{\frac{ds}{\pi}}$.

2.3.2 | Thermal model

The absorbed power density field, $Q(\mathbf{r})$, was calculated from the pressure field, $p(\mathbf{r})$, according to:

$$Q(\mathbf{r}) = \alpha \frac{|p(\mathbf{r})|^2}{\rho c} . \quad (4)$$

Pennes' bioheat transfer equation[62] was applied to calculate the 3D temperature distribution[10,11,64] resulting from the heat source, $Q(\mathbf{r})$, as follows:

$$\rho\, C \frac{\partial\, T(\mathbf{r}, t)}{\partial\, t} = \nabla.[\kappa\, \nabla T(\mathbf{r}, t)] - \omega\, \rho_B\, C_B\, [T(\mathbf{r}, t) - T_B] + Q(\mathbf{r}) . \quad (5)$$

Here, $T(\mathbf{r}, t)$ represents the temperature field at time t, C, κ and ω denote the voxel-wise specific heat capacity, thermal conductivity, and perfusion rate of the given tissue type, whereas ρ_B and C_B denote the density and specific heat capacity of blood, respectively. The initial body temperature and blood temperature (T_B) were both set to 37 °C for all thermal simulations. In bone regions (i.e., hip and spine), Equation 4 was computed as the sum of the absorbed power density fields associated with the longitudinal and shear wave components.[69,70] Thermal dose fields were computed[71] and ablation volumes were estimated as the volume of tissue receiving a thermal dose greater than or equal to 240 cumulative equivalent minutes at 43 °C (CEM_{43}).

2.4 | Numerical implementation

For each patient simulated in this study, the orientation of the transducer array relative to the patient's anatomy during their clinical treatment was replicated in silico. The transducer's array elements were discretized spatially at $(\lambda/6)^2$, as were the water membrane and various tissue layer boundaries. In the thermal model, the voxel size was $\lambda/6$ isotropic and the time step was set to 43.2 ms, the latter of which was sufficiently short to satisfy the von Neumann stability condition.[72] Within the focal region, pressure and temperature fields were calculated over a 30 mm × 30 mm × 30 mm domain, whereas in the near-hip and near-spine regions adaptive domain sizes were necessary depending on the patient's anatomy (approx. 60 mm × 115 mm × 185 mm in spine, 45 mm × 50 mm × 45 mm in hip). Following a previous simulation study of MRgFUS for uterine fibroids,[11] low particle velocity magnitudes were not propagated from layer to layer to reduce processing time without altering the outcome substantially. Ignoring velocities less than 5% of the spatial-peak velocity on a given layer produced a mean change of less than 2% across the resulting 3D pressure field (<0.1% change in the peak pressure), while cutting processing times in half. We applied this approximation both when propagating velocities from layer to layer and when computing the resulting 3D pressure fields.

2.5 | Module blocking and simulated sonications

A transducer module blocking algorithm was developed to estimate which modules within the phased array have beams that intersect no-pass zones for a given sonication target. For each transducer module, a volumetric beam through the target extending 6 cm past the target was generated. The beam was a module-sized square (12 mm × 12 mm) at the transducer surface, converged down to a point at the target, and diverged at the same angle past the target. Array elements within modules whose beam intersected with any tissue layer surface area sub-element of a no-pass zone (i.e., bone, bowel) were blocked. This procedure was carried out for all 96 transducer modules within the array. Different blocking percentage values were tested for modules intersecting with no-pass bone regions (i.e., hips and spine), whereby the transducer element output power levels within blocked modules were reduced by the corresponding blocking percentage value. In addition to the no blocking (i.e., blocking percentage = 0%) and full-blocking (i.e., blocking percentage = 100%, elements turned off) scenarios, we investigated four intermediate partial blocking percentages (20%, 40%, 60%, 80%), each of which resulted in a binary distribution of output power levels across the array. Transducer modules with beams intersecting no-pass bowel regions were always blocked fully (i.e., blocking percentage = 100%), to mimic the patient treatments.[7] Figure 1c shows an example of a hypothetical treatment point in proximity to the bowel, illustrating the calculation of blocked modules.

Investigating near-bone sonications across multiple patients required a standardized approach to treatment point selection. In this study, we only tested target locations with at least 50% of the total array modules unblocked, so as to not drastically reduce the active array aperture. For each patient, we determined the point along the vector connecting the center point of the array to the closest point on the bone surface of interest (i.e., spine or hip) that resulted in as close to 48 of 96 blocked modules within the array as possible without exceeding 50%. We then placed up to 3 additional targets proximal to the transducer along that vector in steps of 5 mm, provided the target and resulting focal heating volume were contained within the patient's fibroid. We simulated a total of 73 targets across all 10 patients (Table 2). Sonications near both the left and right hip bones were each tested in half of the patient population (right: patients #1/4/5/7/8, left: patients #2/3/6/9/10).

TABLE 2 Number of blocked modules within the array due to the no-pass bone region (spine/hip) for simulated sonications across all patients.

Location \ Patient	#1	#2	#3	#4	#5	#6	#7	#8	#9	#10
#1	48/48	48/48	48/48	48/48	48/48	47/48	46/46	45/48	47/47	47/47
#2	40/40	37/34	30/39	40/39	37/35	26/38	38/38	31/40	39/40	40/30
#3	27/30	22/25	22/28	25/28	21/26	13/27	21/29	18/32	31/32	31/-
#4	18/21	12/19	-/-	15/-	8/-	1/-	12/13	6/26	16/25	16/-

Note: Locations #1 and #4 are closest to and farthest from the bone surface of interest, respectively.

Table 2 lists the number of blocked modules for each sonication in each patient. Each target was simulated initially without any aberration corrections incorporated into the array element driving phases. The driving phases at the operating frequency ($f = 518$ kHz) for a given target location were calculated assuming propagation within a homogeneous medium ($c_L = 1540$ m/s). Each target was then re-simulated to investigate the impact of soft-tissue phase aberration corrections[73–75] using an analytic ray-tracing approach.[76] In a single patient (#1), additional sonications were simulated at targets placed both near the hip (93 targets) and spine (154 targets) to investigate how close to bone ablative exposures may be feasible using various apodization approaches without phase corrections.

The simulations in this study were carried out on a desktop workstation (AMD Ryzen Threadripper Pro 5975WX processor, 256 GB memory, 32 cores, 64 threads) containing a single NVIDIA GPU (GeForce RTX 4090, 24 GB memory, 16 384 cores). The acoustic and thermal simulations took approximately 20 min (7 min) and 1 min (30 s) to run for a single near-spine (near-hip) target, respectively. In total, 193 near-spine and 127 near-hip target locations were investigated across the 10 patients in this study. The total simulation time, including both acoustic and thermal simulations for all target locations at each of the 6 blocking percentages investigated, including the additional phase correction simulations, was approximately 25 days.

The primary outcome metric of interest in this study was the ratio of the spatial-peak temporal-peak (SPTP) temperature elevation within the focal region (ΔT_{focal}) to the SPTP temperature elevation within the bone[77] (ΔT_{bone}), defined as $\Delta T_{\text{ratio}} = \Delta T_{\text{focal}}/\Delta T_{\text{bone}}$, with higher values translating to more effective treatments. The optimal blocking percentage for a given target was determined as the percentage providing the maximum ΔT_{ratio} value. Focal heating volumes were quantified as the volume of fibroid tissue in which the temperature elevation was greater than or equal to 50% of ΔT_{focal}, with larger values for a fixed target location corresponding to more diffuse focusing. Targeting error was quantified as the Euclidean distance between the intended target and the location of SPTP focal temperature elevation. For each simulated sonication, following transducer module blocking with a given blocking percentage value, the total acoustic power across the array was scaled to achieve $\Delta T_{\text{focal}} = 35\ ^{\circ}\text{C}$ at the end of a 30 s sonication at the target of interest. This normalization facilitated a comparison of both the temperature elevation within bone regions, as well as the total and peak module-wise acoustic power levels required to achieve equivalent levels of focal heating, across different cases. Numerical simulations of this device were found to over-predict the focal intensity obtained in water tank needle hydrophone measurements by a factor of 1.04 ± 0.06 (mean $\pm$ SD) depending on the target location, following correction for the hydrophone's directivity profile,[78] which translated to an underestimation of the powers required to achieve a given level of focal heating in silico compared our clinical experience. In estimating how close to bone ablative exposures may be feasible, sonications with a ΔT_{ratio} value above 4.375 were considered treatable; assuming a resting body temperature of 37°C this threshold corresponds to a peak focal temperature of 72°C (i.e., 35 °C elevation), sufficient for thermal coagulation over a 30 s sonication, with a peak bone temperature of 45°C (i.e., 8°C elevation) the upper limit of temperature-induced pain thresholds.[79] The bone stand-off distance with a 50% predicted outcome of being classified as treatable (D_{50}) was obtained via probit analysis.[80]

3 | RESULTS

Figures 2 and 3 show temperature field data in the focal and bone regions, respectively, from an example sonication near the spine for different module blocking percentage values. Examining the focal region (Figure 2), it can be seen that the focal heating volume generally increases with increasing blocking percentage, corresponding to more diffuse focusing, without impacting the array's targeting capabilities. As the blocking percentage is increased, both the total and peak module-wise acoustic power levels required to achieve the desired focal temperature elevation also increase due to the reduced effective aperture. In the spine region (Figure 3), variable levels of bone heating are observed for different blocking percentage values. For this target,

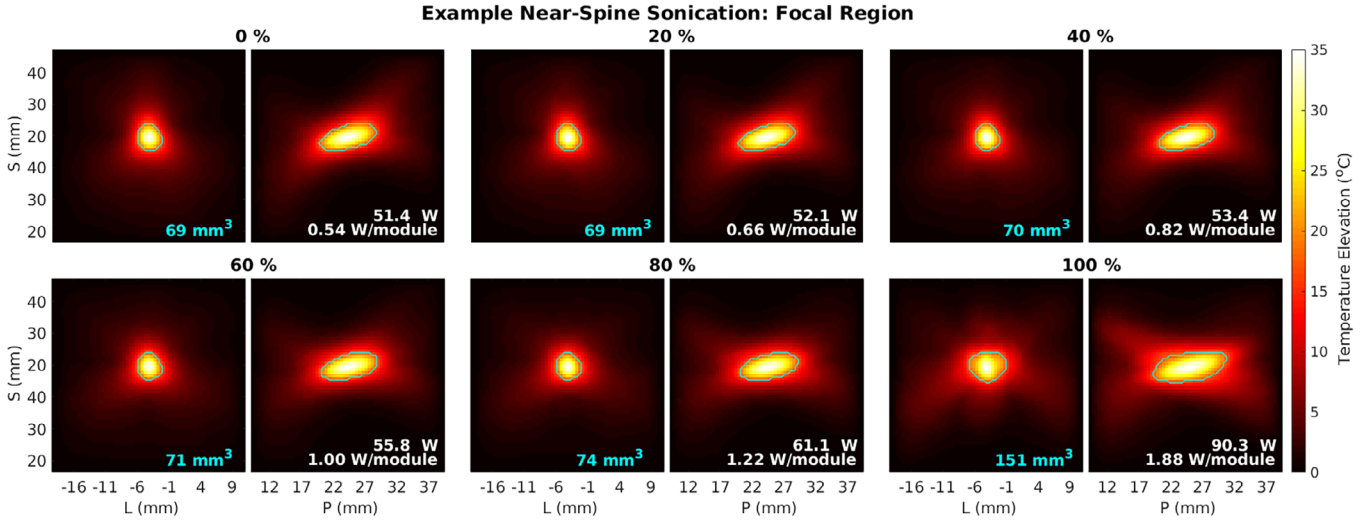

FIGURE 2 Temporal-peak coronal (L-S, left plots) and sagittal (P-S, right plots) maximum intensity projection temperature field distributions at the focus for an example sonication near spine (patient #1, target 33 mm from spine, no phase corrections), with different blocking percentages. 48 of the 96 transducer modules had beams that intersected the no-pass spine region. Total and peak module-wise acoustic power levels required to achieve the fixed $\Delta T_{focal} = 35°C$ value for each case are listed as insets (white, sagittal) along with the focal heating volumes (cyan, coronal). Cyan contours denote regions where the temperature elevation exceeds 50% of ΔT_{focal}. L = left, P = posterior, S = superior.

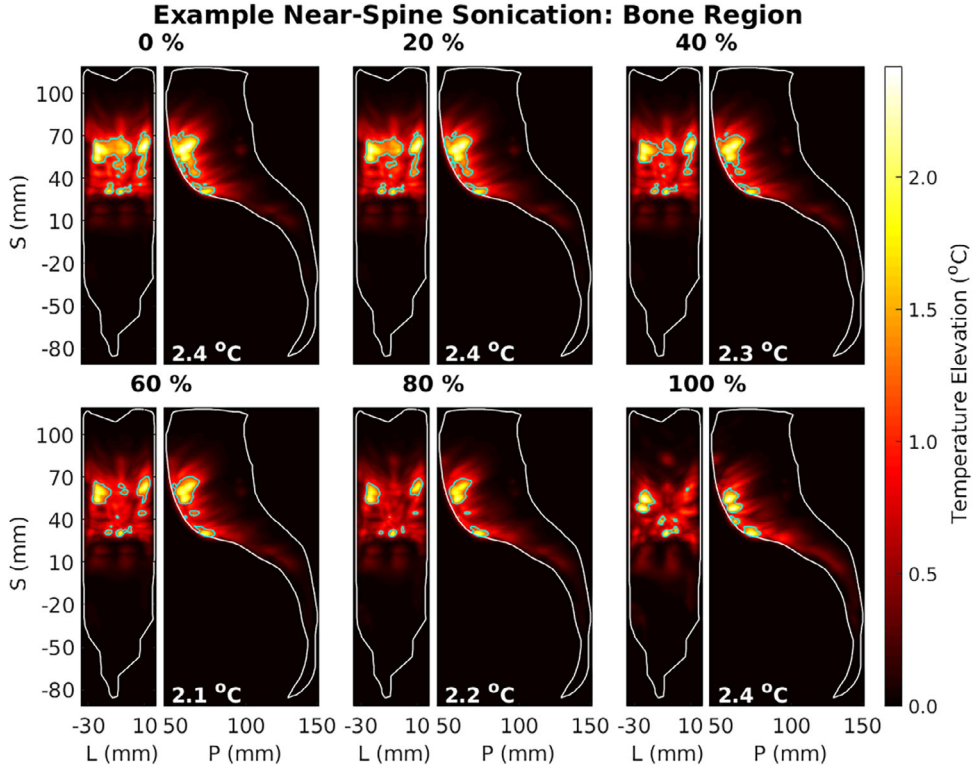

FIGURE 3 Temporal-peak coronal (L-S, left plots) and sagittal (P-S, right plots) maximum intensity projection temperature field distributions within the bone region for an example sonication near spine (patient #1, target 33 mm from spine, no phase corrections), with different blocking percentages. 48 of the 96 transducer modules had beams that intersected the no-pass spine region. ΔT_{bone} values are listed as insets (white, sagittal). Cyan contours denote regions where the temperature elevation exceeds 50% of ΔT_{bone}. White contours denote the spine region. L = left, P = posterior, S = superior.

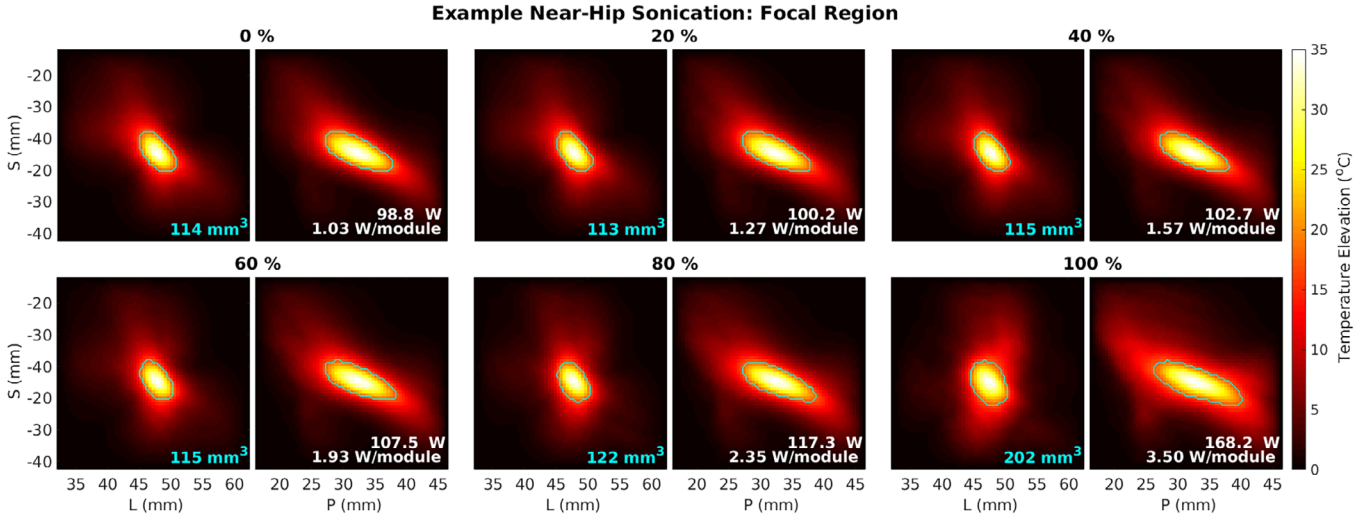

FIGURE 4 Temporal-peak coronal (L-S, left plots) and sagittal (P-S, right plots) maximum intensity projection temperature field distributions at the focus for an example sonication near hip (patient #2, target 25 mm from hip, no phase corrections), with different blocking percentages. 48 of the 96 transducer modules had beams that intersected the no-pass hip region. Total and peak module-wise acoustic power levels required to achieve the fixed $\Delta T_{focal} = 35°C$ value for each case are listed as insets (white, sagittal) along with the focal heating volumes (cyan, coronal). Cyan contours denote regions where the temperature elevation exceeds 50% of ΔT_{focal}. L = left, P = posterior, S = superior.

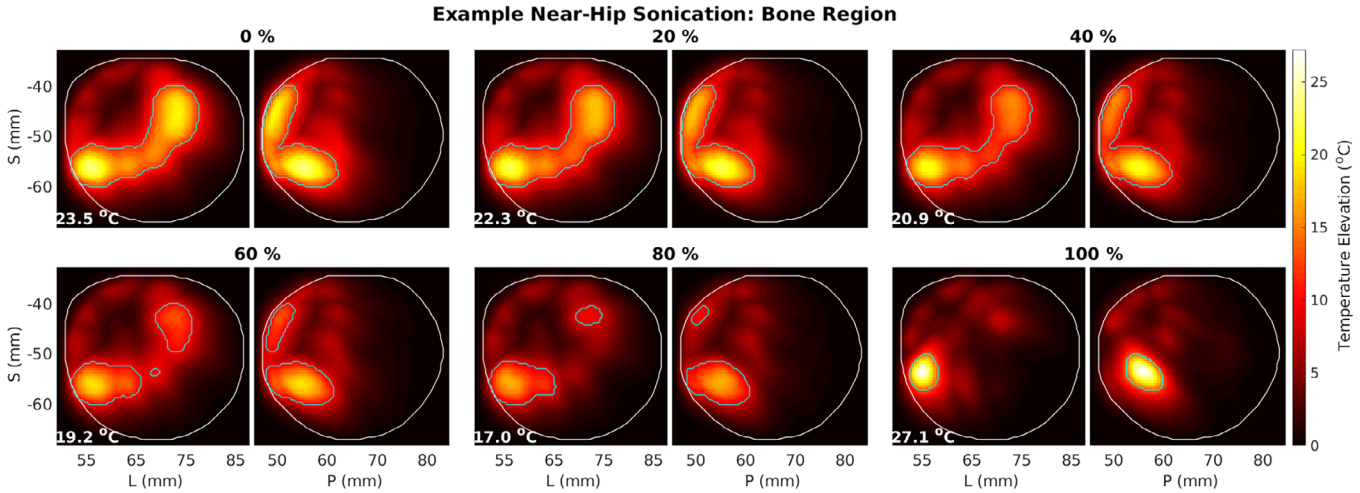

FIGURE 5 Temporal-peak coronal (L-S, left plots) and sagittal (P-S, right plots) maximum intensity projection temperature field distributions within the bone region for an example sonication near hip (patient #2, target 25 mm from hip, no phase corrections), with different blocking percentages. 48 of the 96 transducer modules had beams that intersected the no-pass hip region. ΔT_{bone} values are listed as insets (white, sagittal). Cyan contours denote regions where the temperature elevation exceeds 50% of ΔT_{bone}. White contours denote the hip region. L = left, P = posterior, S = superior.

the peak bone temperature elevation was minimal for a blocking percentage of 60% (SPTP bone temperature elevation = 2.1 °C). For this blocking percentage value, relative to the no blocking case the focal heating volume was increased by 3% (69 mm^3 vs. 71 mm^3), and the required total and peak module-wise acoustic power levels were elevated by 9% (51.4 W vs. 55.8 W) and 85% (0.54 W/module vs. 1.0 W/module), respectively.

Figures 4 and 5 show temperature field data in the focal and bone regions, respectively, from an example sonication near the hip for different module blocking percentage values. Similar to the spine case, focal heating volume was found to increase with increasing blocking percentage in general, without impacting the array's targeting capabilities (Figure 4). As the blocking percentage is increased, both the total and peak module-wise acoustic power levels required to achieve the desired focal temperature elevation also increase. This near-hip target had a greater focal distance (8.7 cm; 6.6 cm depth, 5.7 cm off-axis steering) compared to the near-spine sonication in Figure 2 (6.8 cm; 6.0 cm depth, 3.2 cm

off-axis steering), resulting in more diffuse focusing such that both the focal heating volume and required acoustic power values were elevated in this case. Variable levels of bone heating are observed in the hip (Figure 5) for different blocking percentage values. For this target, the peak bone temperature elevation was minimal for a blocking percentage of 80% (SPTP bone temperature elevation = 17.0 °C). For this blocking percentage value, relative to the no blocking case the focal heating volume was increased by 7% (114 mm^3 vs. 122 mm^3), and the required total and peak module-wise acoustic power levels were elevated by 19% (98.8 W vs. 117.3 W) and 128% (1.03 W/module vs. 2.35 W/module), respectively.

Figure 6 provides summary data for our simulation findings from treatment points located near the spine without employing phase aberration correction. Across all patients, the ΔT_{ratio} was found to decrease as the target was placed closer to the spine. The blocking percentage value that maximized the ΔT_{ratio} varied depending on both the patient and the treatment location. In 62% of near-spine sonications (24/39), the full blocking approach (i.e., turning off elements within transducer modules intersecting with bone) resulted in the maximum ΔT_{ratio}, with a mean (min/max) improvement of 49% (8%/106%) compared to the no blocking case. The required total and peak module-wise acoustic power levels for full blocking were elevated by 37% ± 17% and 101% ± 56% (mean ± SD), respectively, compared to the no blocking case (Figure S1). Among the remaining near-spine sonications, the optimal partial blocking percentage for a given target provided a mean (min/max) improvement of 15% (3%/46%) in ΔT_{ratio} compared to the full blocking approach, and resulted in a mean (min/max) decrease of 34% (5%/56%) in the focal heating volume. In general, both increasing the blocking percentage value and increasing the electronic beam steering distance (i.e., increasing the target's proximity to the spine) resulted in increased focal heating volumes (Figure S2) and ablation volumes (Figure S3). The mean (min/max) targeting error across all spine sonications using the optimal blocking percentage was 1.2 mm (0.6 mm/2.1 mm) (Figure S4).

Figure 7 provides summary data for our simulation findings from treatment points located near the hip without employing phase aberration correction. At the optimal blocking percentage, the ΔT_{ratio} values obtained in the hip were generally lower than those observed in the spine, by a factor of 3.4 ± 2.6 on average (Table 3). Similar to the spine case, ΔT_{ratio} was found to decrease as the target was placed closer to the hip across all patients. The blocking percentage value that maximized the ΔT_{ratio} also varied depending on both the patient and the treatment location in the hip. In 50% of near-hip sonications (17/34), the full blocking approach (i.e., turning off elements within transducer modules intersecting with bone) resulted in the maximum ΔT_{ratio}, with a mean (min/max) improvement of 82% (7%/158%) compared to the no blocking case. The required total and peak module-wise acoustic power levels for full blocking were elevated by 6%±17% and 65%±36% (mean ± SD), respectively, compared to the no blocking case (Figure S5). Among the remaining near-hip sonications, the optimal partial blocking percentage for a given target provided a mean (min/max) improvement of 29% (1%/102%) in ΔT_{ratio} compared to the full blocking approach, and resulted in a mean (min/max) decrease of 20% (2%/40%) in the focal heating volume. In general, both increasing the blocking percentage value and increasing the electronic beam steering distance (i.e., increasing the target's proximity to hip) resulted in increased focal heating volumes (Figure S6) and ablation volumes (Figure S7). The mean (min/max) targeting error across all hip sonications using the optimal blocking percentage was 1.5 mm (0.5 mm/2.7 mm) (Figure S8).

Figure 8 shows representative near-spine and near-hip sonications demonstrating the impact of incorporating element-wise phase aberration corrections into the array driving signals. When using the optimal blocking percentage for a given treatment scenario, phase corrections improved the resulting average focal quality relative to the no correction case, reducing the focal heating volumes (13% ± 21%/18% ± 14% decrease for spine/hip targets, mean ± SD), required total power levels (7% ± 14%/8% ± 12% decrease for spine/hip targets, mean ± SD), and targeting errors (41% ± 22%/22% ± 40% decrease for spine/hip targets, mean ± SD) (Figure 9). Although phase corrections improved ΔT_{ratio} values on average (35% ± 24%/52% ± 47% increase for spine/hip targets, mean ± SD), they did not do so at each individual target location investigated, with 7% of cases (5/73 targets) suffering a reduction in ΔT_{ratio} (Figure 9). Further, in 49% of cases (36/73 targets) the optimal blocking percentage with phase corrections was different than that obtained from geometric focusing (i.e., without phase corrections). Plots of various outcome metrics for each target location simulated with phase aberration corrections are provided in the supplemental materials (Figures S9–S18).

Figure 10 illustrates the target locations simulated to evaluate near-bone treatments. Full module blocking was found to increase the transducer array's treatment envelope compared to the no blocking control case, with D_{50} dropping from 42 ± 1 mm (17 ± 2 mm) to 38 ± 1 mm (8 ± 1 mm) for sonications near hip (spine). Optimal module blocking provided further improvements in the treatment envelope relative to the full blocking case (D_{50} = 36 ± 1 mm near hip and 7 ± 1 mm near spine). Near-hip sonications classified as treatable in this patient resulted in mean thermal dose volumes

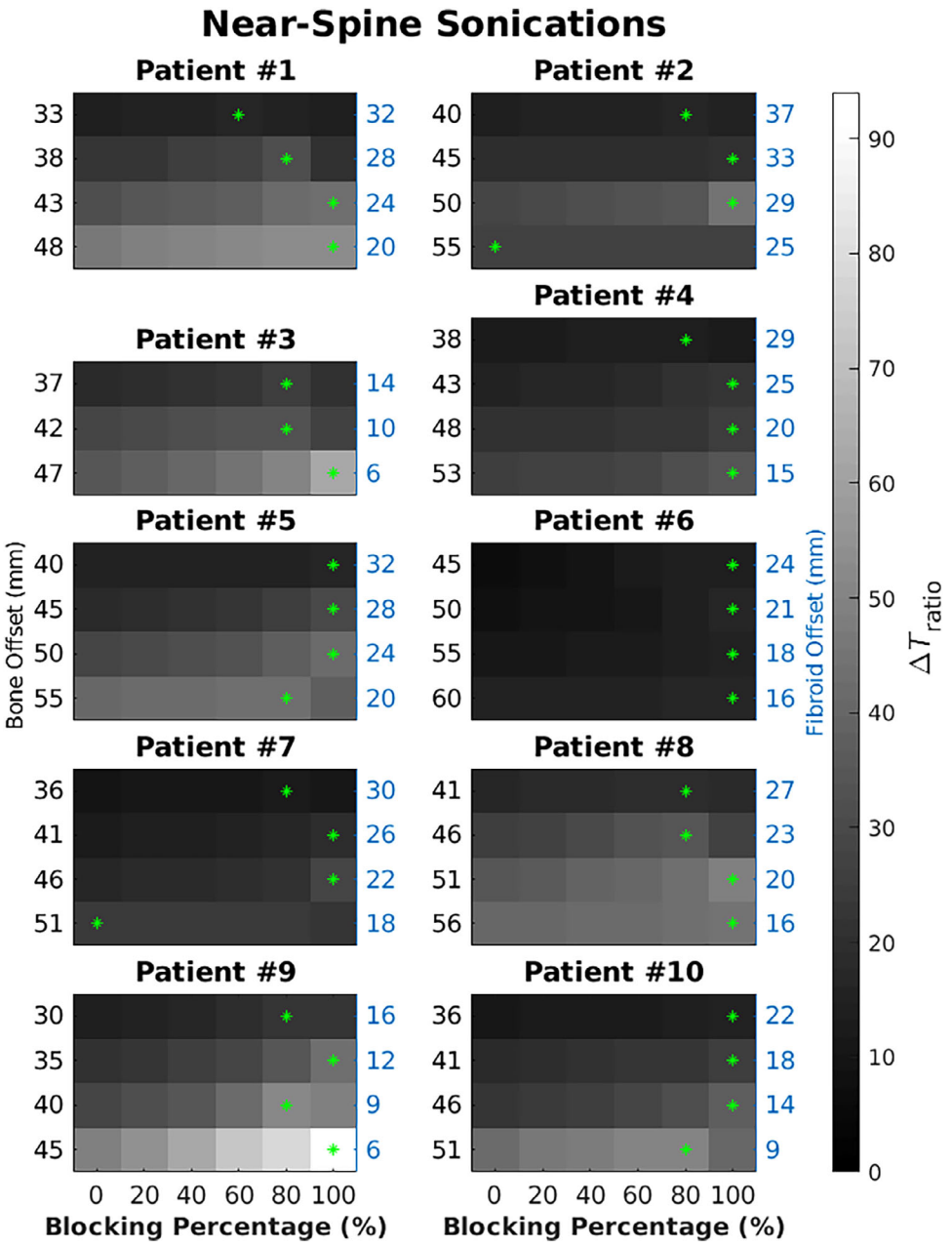

FIGURE 6 ΔT_{ratio} values ($\Delta T_{focal}/\Delta T_{bone}$) for all near-spine sonications across ten patients (no phase corrections). The offset distance from the treatment point to the spine surface is provided on the left y-axis in black and from the treatment point to the muscle-fibroid boundary layer on the right y-axis in blue. Green asterisks denote the power-based blocking percentage resulting in the maximum ΔT_{ratio} for each target.

TABLE 3 Maximum ΔT_{ratio} values (spine/hip) for simulated sonications across all patients without phase correction (i.e., green asterisks in Figures 6 and 7).

Location \ Patient	#1	#2	#3	#4	#5	#6	#7	#8	#9	#10
#1	16.3/4.0	16.8/2.1	25.8/4.4	14.2/2.6	16.2/5.1	14.7/5.7	12.0/4.2	20.4/3.5	23.4/3.6	15.2/10.3
#2	31.9/6.2	21.1/3.2	32.5/8.4	22.8/7.6	30.3/8.0	17.4/11.6	19.2/14.5	34.7/6.2	42.8/5.7	25.2/10.7
#3	43.4/10.6	44.7/6.4	62.3/16.4	25.5/13.5	42.2/18.2	15.4/17.8	28.8/11.0	49.8/11.3	52.8/8.4	37.2/-
#4	54.2/13.6	27.9/14.2	-/-	34.8/-	43.5/-	17.6/-	24.8/14.1	45.2/22.3	94.0/16.8	51.2/-

Note: Locations #1 and #4 are closest to and farthest from the bone surface of interest, respectively.

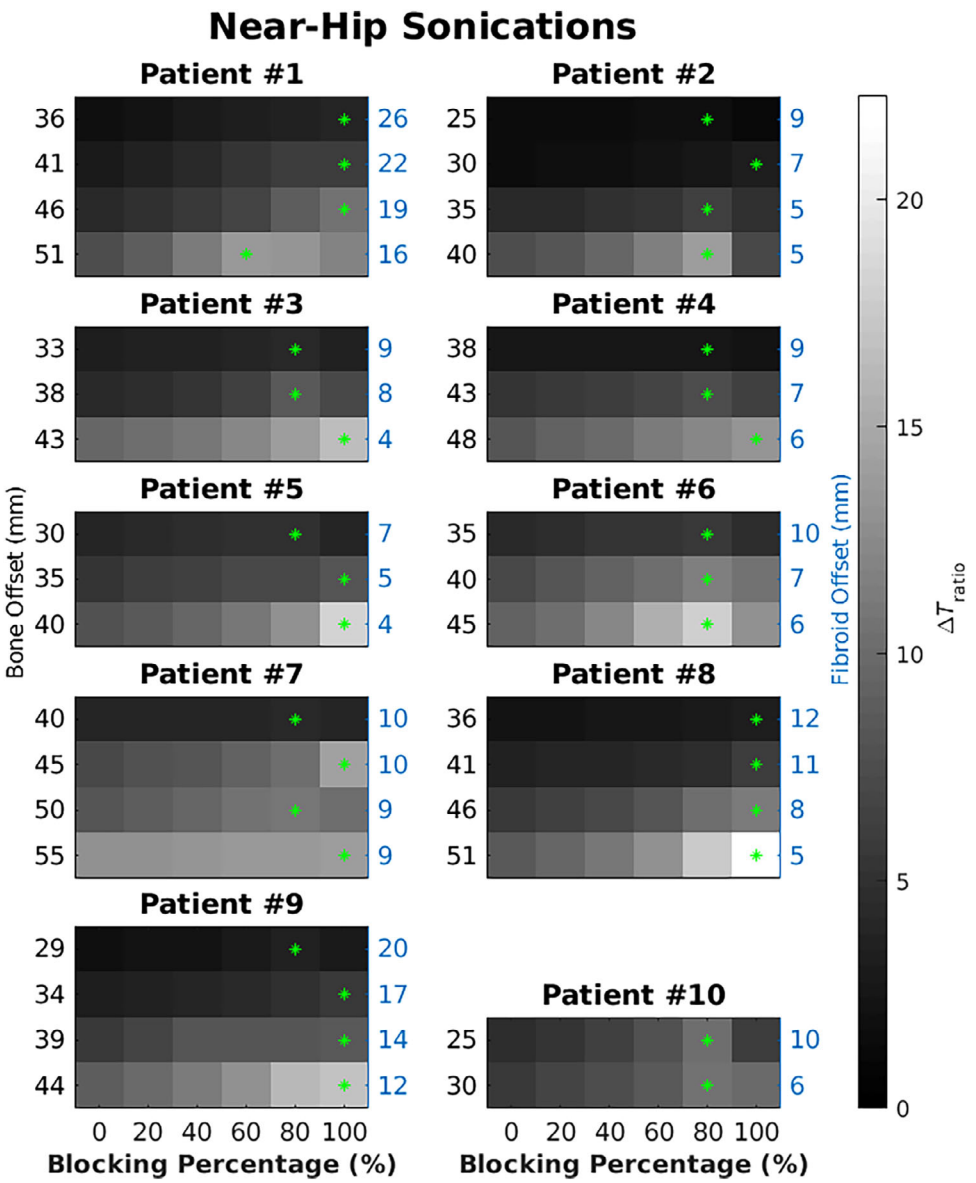

FIGURE 7 ΔT_{ratio} values ($\Delta T_{focal}/\Delta T_{bone}$) for all near-hip sonications across ten patients (no phase corrections). The offset distance from the treatment point to the hip surface is provided on the left *y*-axis in black and from the treatment point to the muscle-fibroid boundary layer on the right *y*-axis in blue. Green asterisks denote the power-based blocking percentage resulting in the maximum ΔT_{ratio} for each target.

of 160 ± 30 mm^3 (no blocking, 15 of 93 targets), 250 ± 160 mm^3 (full blocking, 47 of 93 targets), and 230 ± 140 mm^3 (optimal blocking, 55 of 93 targets) at the focus. Near-spine sonications classified as treatable in this patient resulted in mean thermal dose volumes of 150 ± 30 mm^3 (no blocking, 43 of 154 targets), 250 ± 60 mm^3 (full blocking, 103 of 154 targets), and 220 ± 50 mm^3 (optimal blocking, 106 of 154 targets) at the focus. The peak thermal dose values deposited in bone for treatable near-hip and near-spine sonications were both less than 1 CEM_{43}, below the thresholds for irreversible damage to bone or its surrounding soft tissues.[81] Although sensitivity to heat is highly variable across different tissue types, in general, a thermal dose of 10–20 CEM_{43} is needed to induce thermal damage.[82]

4 | DISCUSSION

The findings from this simulation study suggest that, when ablating fibroid tissue using a 6144-element flat fully-populated phased array system operating at 0.5 MHz, for equivalent levels of focal heating transducer module blocking reduces bone heating compared to the no blocking control case, at the cost of more diffuse focusing and thus requiring elevated total and peak per-module acoustic power levels. Furthermore, in

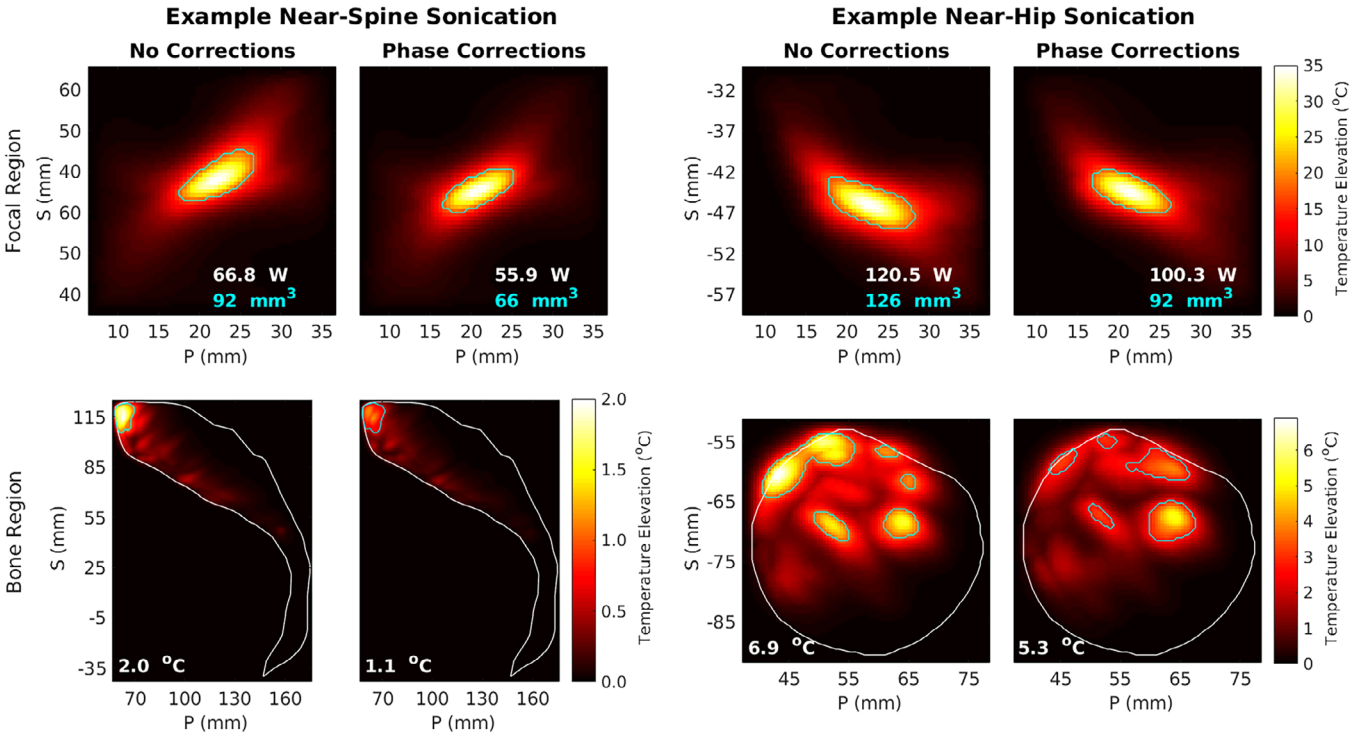

FIGURE 8 Sagittal temporal-peak maximum intensity projection temperature field distributions within the focal and bone regions for representative near-spine (patient #6, location #4) and near-hip (patient #5, location #1) sonications, both with (optimal blocking percentages = 100%/80% for spine/hip) and without (optimal blocking percentages = 100%/80% for spine/hip) the inclusion of phase corrections into the array driving signals. Total acoustic power levels required to achieve the fixed $\Delta T_{focal} = 35°C$ value for each case (white) and focal heating volumes (cyan) are listed as insets (focal region), as well as the ΔT_{bone} values (bone region, white). Cyan contours denote regions where the temperature elevation exceeds 50% of the spatial-peak temperature elevation within the region of interest (i.e., focal or bone). P = posterior, S = superior.

just under half of simulated sonications partial module blocking was shown to provide improvements in both the ratio of focal-to-bone heating and the focal heating volume relative to the full blocking case. The optimal blocking percentage value was found to be dependent on the specific patient geometry and target location of interest, as well as whether or not phase aberration corrections were employed, suggesting that pretreatment simulations incorporated within the treatment planning workflow will be necessary to fully exploit this strategy during clinical MRgFUS treatments. Preliminary results suggest this transducer module apodization approach may facilitate the ablation of fibrous tissues closer to bony structures, thereby increasing the treatment envelope of MRgFUS surgery in the body. MRgFUS-based thermoablation of other targets within the abdomen (e.g., liver,[83,84] kidney,[85] pancreas[86]) may also benefit from similar techniques.

Although the improvements obtained in the focal-to-bone heating ratio provided by transducer module apodization translated to increased effective treatment envelopes, they came at the cost of requiring elevated total and peak per-module acoustic power levels to match the focal heating of the no blocking control case. The MRgFUS system investigated in this work is fully capable of delivering adequate power to compensate for these more stringent power requirements (upwards of 800 W operating in continuous wave mode, consistent with 6–10 W per module[12]). Transducer module apodization also resulted in marginal increases of the focal heating volume relative to the no blocking case (7% ± 12%/25% ± 27% mean and 55%/98% maximum increase vs. no blocking at the optimal blocking percentage in hip/spine), which are small (maximum value = 0.21 cm^3 in both hip and spine [Figures S2, S6]) compared to the large fibroid volumes typically treated via MRgFUS (e.g., fibroid load of 372 ± 235 cm^3 in Stewart et al.[13]). Finally, the phased array's targeting accuracy was found to be unaffected by transducer module apodization, with sub-wavelength worst-case targeting errors at the optimal blocking percentage (Figures S4–S8).

The inclusion of soft-tissue phase aberration corrections into the driving signals improved focusing quality on average, resulting in decreased focal heating volumes, lower total power levels required to achieve a fixed temperature elevation, and reduced targeting errors. A major benefit of the lower transducer driving frequency of this device relative to alternative MRgFUS systems for uterine fibroid treatments is the reduced impact of

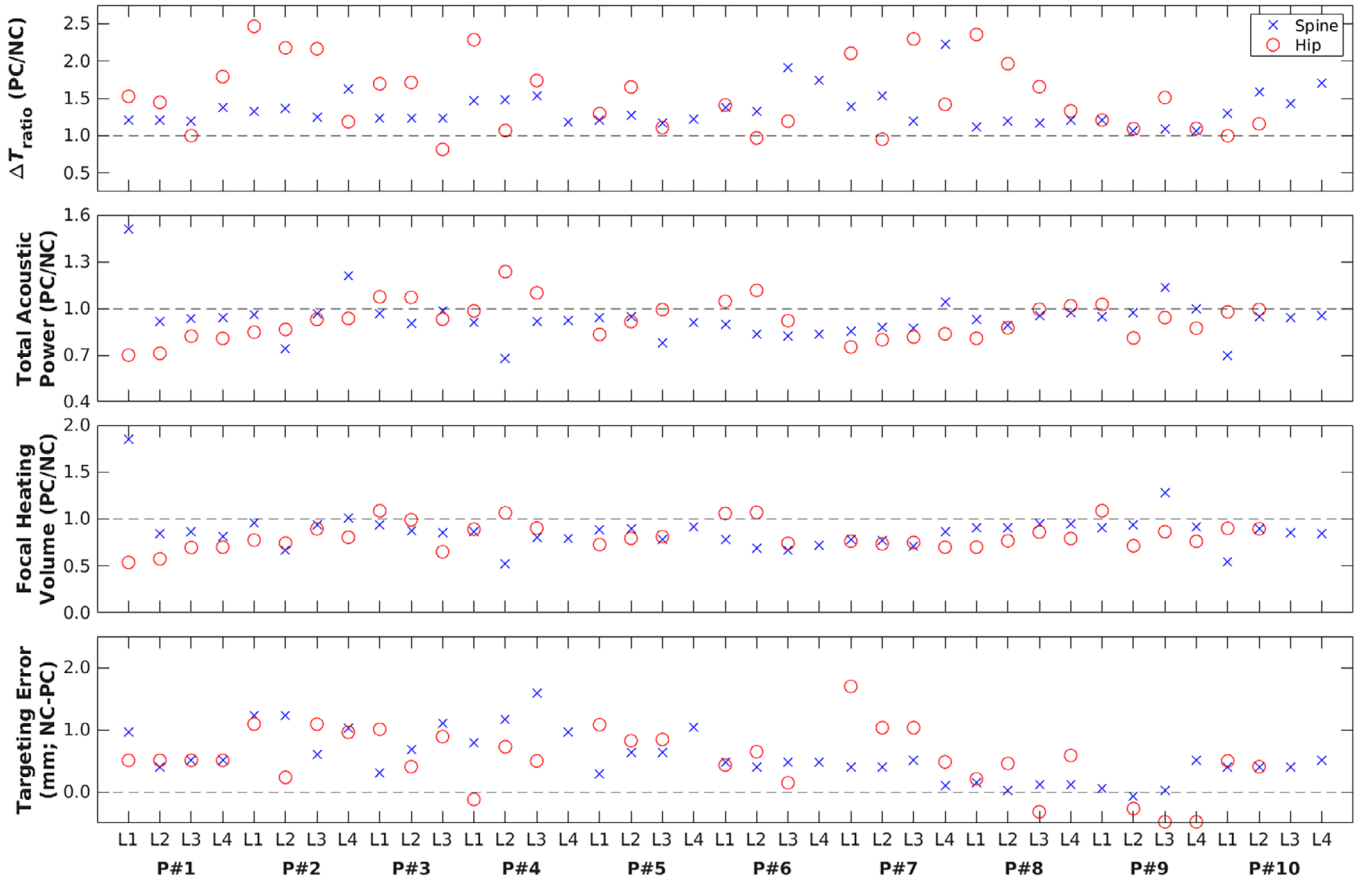

FIGURE 9 Improvement of different performance metrics (ΔT_{ratio}, total acoustic power, focal heating volume, and targeting error) obtained with PC relative to the corresponding NC case for all sonications simulated across ten patients. Metrics are plotted for the optimal blocking percentage for each treatment scenario (i.e., patient, location, driving signals), and are presented as either a ratio (PC/NC) or difference (NC-PC) between the two cases. Horizontal dashed lines indicate no change between the PC and NC cases. L1-L4 denote target locations #1–4, and P#1–10 denote patients #1–10. NC, no correction; PC, phase correction.

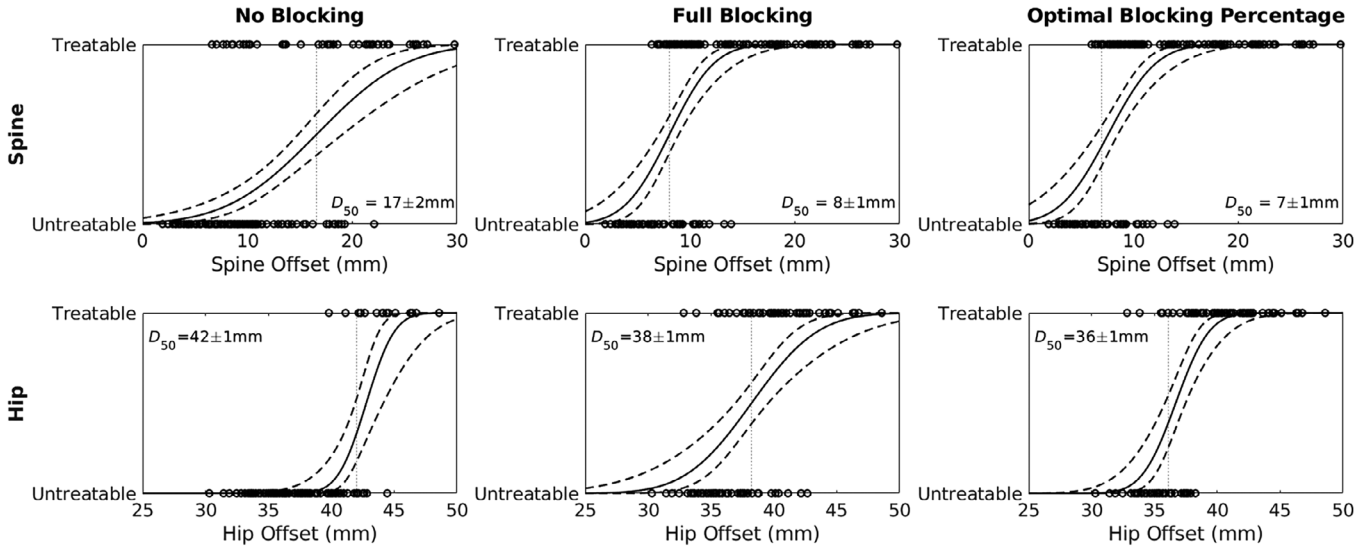

FIGURE 10 Simulated sonications near spine (top row) and hip (bottom row) in patient #1, stratified into treatable and untreatable sonications as a function of the offset distance to bone (no phase corrections). Probit regression (solid line) with 95% confidence intervals (dashed lines) along with the D_{50} distance (dotted line) are shown for each case.

soft-tissue field distortions arising from trans-abdominal propagation.[38] Nevertheless, phase corrections could therefore be used to help counteract the focal quality reductions that result from transducer module blocking. Although phase corrections were also found to improve the focal-to-bone heating ratio on average, it is worth noting that they did not do so at each individual location investigated. Further, it was also shown that phase corrections impacted the optimal blocking percentage for a given treatment scenario. Taken together, these results highlight the need for a priori simulations to fully exploit this approach in a clinical setting.

The simulated improvements provided by the proposed modular transducer apodization approach are expected to over-estimate its performance in practice for several reasons, including inaccurate soft tissue boundary segmentation, the potential for patient motion occurring between the end of MRI acquisition and prior to the delivery of simulation-informed FUS exposures, as well as uncertainties in tissue-specific acoustic/thermal properties in patients. Implementation of MR[87] or ultrasound[88,89] imaging-based methods for tracking and compensating for unwanted patient motion may help in this regard, particularly if aberration corrections are to be employed. Furthermore, accurate determination of which transducer modules should be blocked plays a central role in our proposed method. Although we assumed straight line-of-sight propagation to determine blocked transducer modules in this work, acoustic waves propagating within the body will deviate from this ideal approximation as a result of spatial tissue inhomogeneities. We also employed a fixed 6 cm far-field cut-off distance in our algorithm to avoid over-blocking transducer modules, however, this choice of distance will greatly impact outcomes and should be studied in greater detail in the future. Experimental verification and validation of the proposed methodology is therefore warranted to evaluate its performance in vivo.

The development of rapid methods for both MRI-based tissue layer segmentation and acoustic/thermal field simulations will be required prior to routine clinical adoption of this approach, to minimize the time between the end of MRI acquisition and delivery of the simulation-informed ultrasound exposures. In this work, MRI-based segmentation was performed manually on a slice-by-slice basis and was relatively time-consuming, taking several hours to complete a single patient. Recent advancements in automated abdominal soft-tissue segmentation via deep learning approaches represent potential solutions to this problem.[90,91] Following MRI-based tissue segmentation, the total computational time associated with acoustic and thermal simulations for one near-spine sonication and one near-hip sonication in a given patient was approximately 30 min, despite using GPU-based model implementations.[92,93] Neural network-based field generation techniques,[94] more sophisticated computing hardware,[95,96] as well as simulation acceleration techniques (e.g., simulating lower transmit frequencies,[97] decreasing the surface mesh discretization density[98]) could help decrease the associated computational times in the future. To be practical in a clinical setting, the total time for segmentation and simulation will need to be reduced to on the order of a few minutes.

In this proof-of-principle study, a relatively coarse step size of 20% was chosen when investigating different power-based partial blocking percentages, however, a finer step size may lead to even further improvements in the future. In addition, the proposed apodization approach adjusts transducer amplitudes on a module-wise basis (i.e., 64-elements at a time), but in practice each of the phased array's individual 6144 elements can be driven with a unique amplitude and phase,[7] providing the opportunity to exploit a greater number of degrees of freedom. Future work will investigate element-wise phase and amplitude control for the delivery of optimal energy deposition patterns, such as the application of anti-foci points[77,99,100] within no-pass zones.

5 | CONCLUSION

Numerical simulations of uterine fibroid ablation near hip and spine regions using a 6144-element flat, fully-populated MRgFUS phased array operating at 0.5 MHz, suggest that transducer module blocking based on beam intersections with no-pass zones within the field can help increase the ratio of focal-to-bone heating compared to the no blocking control case, at the cost of more diffuse focusing and thus requiring elevated total and per-module acoustic powers to achieve equivalent levels of focal heating. In just under half of simulated sonications partial module blocking provided further improvements relative to the full blocking case, both in terms of the focal-to-bone heating ratio as well as the focal heating volume. The optimal blocking percentage value was dependent on the specific patient geometry and target location of interest. Although not all target locations saw benefit, soft-tissue phase aberration corrections provided improvements in the average focal-to-bone heating ratio and impacted the optimal blocking percentage value for a given treatment scenario. Transducer module blocking enabled tissue ablation closer to bony structures without overheating or damaging the bone, with the partial blocking approach facilitating treatments in the closest proximity to both the hips and spine. The proposed transducer apodization scheme shows promise for improving treatment planning for MRgFUS surgery of uterine fibroids and, more generally, increasing the effective treatment envelope of MRgFUS within the body.

ACKNOWLEDGMENTS

The authors would like to thank M. Hyvärinen (Sunnybrook Research Institute) and B. Lucht (Arrayus Technologies) for providing technical support. Financial support for this work was provided by the Strategic Innovation Fund, the Ontario Research Fund, Arrayus Technologies, and the Temerty Chair in Focused Ultrasound Research at Sunnybrook Health Sciences Centre.

CONFLICT OF INTEREST STATEMENT

K.H. is the founder and board chair of Arrayus Technologies. R.M.J. has received consulting fees from Arrayus Technologies.

REFERENCES

1. Stewart EA, Laughlin-Tommaso SK, Catherino WH, Lalitkumar S, Gupta D, Vollenhoven B. Uterine fibroids. *Nat Rev Dis Primers*. 2016;2:16043.
2. Eden RC, Andrew DC, Nicole KB, Melinda BH, Barbara JS, James HS. The estimated annual cost of uterine leiomyomata in the United States. *Am J Obstet Gynecol*. 2012;206:211.e1-211.e9.
3. Wang W, Liu W, Zhou J, Xu J, Gai L, Huang C. Treatment of symptomatic uterine leiomyomata with high intensity focused ultrasound: a preliminary clinical study. *Chin J Ultrason*. 2002;11:161-163.
4. Tempany CMC, Stewart EA, McDannold N, Quade BJ, Jolesz FA, Hynynen K. MR imaging–guided focused ultrasound surgery of uterine leiomyomas: a feasibility study. *Radiology*. 2003;226:897-905.
5. McDannold N, Tempany CM, Fennessy FM, et al. Uterine leiomyomas: MR imaging–based thermometry and thermal dosimetry during focused ultrasound thermal ablation. *Radiology*. 2006;240:263-272.
6. Zhang L, Chen WZ, Liu YJ, et al. Feasibility of magnetic resonance imaging-guided high intensity focused ultrasound therapy for ablating uterine fibroids in patients with bowel lies anterior to uterus. *Eur J Radiol*. 2010;73:396-403.
7. Aslani P, Huang Y, Lucht BBC, et al. A fully electronically steerable therapeutic ultrasound phased array with MR-guidance. *IEEE Trans Biomed Eng*. 2024;71:574-582.
8. Köhler MO, Mougenot C, Quesson B, et al. Volumetric HIFU ablation under 3D guidance of rapid MRI thermometry. *Med Phys*. 2009;36:3521-3535.
9. Hynynen K, Jones RM. Image-guided ultrasound phased arrays are a disruptive technology for non-invasive therapy. *Phys Med Biol*. 2016;61:R206-R248.
10. Ellens NPK, Pulkkinen A, Song J, Hynynen K. The utility of sparse 2D fully electronically steerable focused ultrasound phased arrays for thermal surgery: a simulation study. *Phys Med Biol*. 2011;56:4913-4932.
11. Ellens NPK, Hynynen K. Simulation study of the effects of near- and far-field heating during focused ultrasound uterine fibroid ablation using an electronically focused phased array: a theoretical analysis of patient safety. *Med Phys*. 2014;41:072902.
12. Ellens NPK, Lucht BBC, Gunaseelan ST, Hudson JM, Hynynen K. A novel, flat, electronically-steered phased array transducer for tissue ablation: preliminary results. *Phys Med Biol*. 2015;60:2195-2215.
13. Stewart EA, Rabinovici J, Tempany CMC, et al. Clinical outcomes of focused ultrasound surgery for the treatment of uterine fibroids. *Fertil Steril*. 2006;85:22-29.
14. Funaki K, Fukunishi H, Sawada K. Clinical outcomes of magnetic resonance-guided focused ultrasound surgery for uterine myomas: 24-month follow-up. *Ultrasound Obstet Gynecol*. 2009;34:584-589.
15. Ikink ME, Voogt MJ, Verkooijen HM, et al. Mid-term clinical efficacy of a volumetric magnetic resonance-guided high-intensity focused ultrasound technique for treatment of symptomatic uterine fibroids. *Eur Radiol*. 2013;23:3054-3061.
16. Kim YS, Kim JH, Rhim H, et al. Volumetric MR-guided high-intensity focused ultrasound ablation with a one-layer strategy to treat large uterine fibroids: initial clinical outcomes. *Radiology*. 2012;263:600-609.
17. Hynynen K, DeYoung D. Temperature elevation at muscle-bone interface during scanned, focused ultrasound hyperthermia. *Int J Hyperthermia*. 1988;4:267-279.
18. Lehmann JF, DeLateur BJ, Warren CG, Stonebridge JS. Heating produced by ultrasound in bone and soft tissue. *Arch Phys Med Rehabil*. 1967;48:397-401.
19. Weeks EM, Platt MW, Gedroyc W. MRI-guided focused ultrasound (MRgFUS) to treat facet joint osteoarthritis low back pain—case series of an innovative new technique. *Eur Radiol*. 2012;22:2822-2835.
20. Napoli A, Mastantuono M, Marincola BC, et al. Osteoid osteoma: MR-guided focused ultrasound for entirely noninvasive treatment. *Radiology*. 2013;267:514-521.
21. Hurwitz MD, Ghanouni P, Kanaev SV, et al. Magnetic resonance-guided focused ultrasound for patients with painful bone metastases: phase III trial results. *J Natl Cancer Inst*. 2014;106:dju082.
22. Hindley J, Gedroyc WM, Regan L, et al. MRI guidance of focused ultrasound therapy of uterine fibroids: early results. *AJR Am J Roentgenol*. 2004;183:1713-1719.
23. Hipp E, Partanen A, Karczmar GS, Fan X. Safety limitations of MR-HIFU treatment near interfaces: a phantom validation. *J Appl Clin Med Phys*. 2012;13:168-175.
24. Yoon SW, Lee C, Cha SH, et al. Patient selection guidelines in MR-guided focused ultrasound surgery of uterine fibroids: a pictorial guide to relevant findings in screening pelvic MRI. *Eur Radiol*. 2008;18:2997-3006.
25. Zaher S, Gedroyc W, Lyons D, Regan L. A novel method to aid in the visualisation and treatment of uterine fibroids with MRgFUS in patients with abdominal scars. *Eur J Radiol*. 2010;76:269-273.
26. Kim YS, Bae DS, Park MJ, et al. Techniques to expand patient selection for MRI-guided high-intensity focused ultrasound ablation of uterine fibroids. *AJR Am J Roentgenol*. 2014;202:443-451.
27. Monteith S, Snell J, Eames M, Kassell NF, Kelly E, Gwinn R. Transcranial magnetic resonance-guided focused ultrasound for temporal lobe epilepsy: a laboratory feasibility study. *J Neurosurg*. 2016;125:1557-1564.
28. Quesson B, Merle M, Köhler MO, et al. A method for MRI guidance of intercostal high intensity focused ultrasound ablation in the liver. *Med Phys*. 2010;37:2533-2540.
29. de Greef M, Schubert G, Wijlemans JW, et al. Intercostal high intensity focused ultrasound for liver ablation: the influence of beam shaping on sonication efficacy and near-field risks. *Med Phys*. 2015;42:4685-4697.
30. Aubry JF, Pernot M, Marquet F, Tanter M, Fink M. Transcostal high-intensity-focused ultrasound: ex vivo adaptive focusing feasibility study. *Phys Med Biol*. 2008;53:2937-2951.
31. Cochard E, Prada C, Aubry JF, Fink M. Ultrasonic focusing through the ribs using the DORT method. *Med Phys*. 2009;36:3495-3503.
32. Botros YY, Ebbini ES, Volakis JL. Two-step hybrid virtual array ray (VAR) technique for focusing through the rib cage. *IEEE Trans Ultrason Ferroelectr Freq Control*. 1998;45:989-1000.
33. Liu H-L, Chang H, Chen W-S, Shih T-C, Hsiao J-K, Lin W-L. Feasibility of transrib focused ultrasound thermal ablation for liver tumors using a spherically curved 2D array: a numerical study. *Med Phys*. 2007;34:3436-3448.

34. Aslani P, Drost L, Huang Y, et al. Thermal therapy with a fully electronically steerable HIFU phased array using ultrasound guidance and local harmonic motion monitoring. *IEEE Trans Biomed Eng*. 2020;67:1854-1862.
35. Song J, Lucht B, and Hynynen K. Large improvement of the electrical impedance of imaging and high-intensity focused ultrasound (HIFU) phased arrays using multilayer piezoelectric ceramics coupled in lateral mode. *IEEE Trans Ultrason Ferroelectr Freq Control*. 2012;59:1584-1595.
36. C,. W. Connor and Hynynen K. Bio-acoustic thermal lensing and nonlinear propagation in focused ultrasound surgery using large focal spots: a parametric study. *Phys Med Biol*. 2002;47:1911-1928.
37. Lipkin M, Hardy JD. Measurement of some thermal properties of human tissues. *J Appl Physiol*. 1954;7:212-217.
38. Liu HL, McDannold N, Hynynen K. Focal beam distortion and treatment planning in abdominal focused ultrasound surgery. *Med Phys*. 2005;32:1270-1280.
39. Yang J, Chiou R, Ruprecht A, Vicario J, MacPhail LA, Rams TE. A new device for measuring density of jaw bones. *Dentomaxillofac Radiology*. 2002;31:313-316.
40. Hinghofer-Szalkay H, Greenleaf JE. Continuous monitoring of blood volume changes in humans. *J Appl Physiol*. 1987;63:1003-1007.
41. Bilaniuk N, Wong GSK. Speed of sound in pure water as a function of temperature. *J Acoust Soc Am*. 2011;93:1609-1612.
42. Moran CM, Bush NL, Bamber JC. Ultrasonic propagation properties of excised human skin. *Ultrasound Med Biol*. 1995;21:1177-1190.
43. Duck FA. *Physical Properties of Tissues: A Comprehensive Reference Book*. Academic Press; 1990.
44. White PJ, Clement GT, Hynynen K. Longitudinal and shear mode ultrasound propagation in human skull bone. *Ultrasound Med Biol*. 2006;32:1085-1096.
45. Goss SA, Johnston RL, Dunn F. Comprehensive compilation of empirical ultrasonic properties of mammalian tissues. *J Acoust Soc Am*. 1978;64:423-457.
46. Connor CW, Hynynen K. Patterns of thermal deposition in the skull during transcranial focused ultrasound surgery. *IEEE Trans Biomed Eng*. 2004;51:1693-1706.
47. Nell DM, Myers MR. Thermal effects generated by high-intensity focused ultrasound beams at normal incidence to a bone surface. *J Acoust Soc Am*. 2010;127:549-559.
48. Henriques FC, Moritz AR. Studies of thermal injury: I. The conduction of heat to and through skin and the temperatures attained therein. A theoretical and an experimental investigation. *Am J Pathol*. 1947;23:530-549.
49. Hand JW, Li Y, Hajnal JV. Numerical study of RF exposure and the resulting temperature rise in the foetus during a magnetic resonance procedure. *Phys Med Biol*. 2010;55:913-930.
50. Dumas A, Barozzi GS. Laminar heat transfer to blood flowing in a circular duct. *Int J Heat Mass Transfer*. 1984;27:391-398.
51. Spells KE. The thermal conductivities of some biological fluids. *Phys Med Biol*. 1960;5:139-153.
52. Mapleson WW. An electric analogue for uptake and exchange of inert gases and other agents. *J Appl Physiol*. 1963;18:197-204.
53. Lassen NA. Muscle blood flow in normal man and in patients with intermittent claudication evaluated by simultaneous Xe^{133} and Na^{24} clearances. *J Clin Invest*. 1964;43:1805-1812.
54. Nyström C, Forssman L, Roos B. Myometrial blood flow studies in carcinoma of the corpus uteri: a preliminary report on the clearance method using xenon 133. *Acta Radiol Ther Phys Biol*. 1969;8:193-198.
55. McAuliffe MJ, Lalonde FM, McGarry D, Gandler W, Csaky K, Trus BL. Medical image processing, analysis and visualization in clinical research. In: *Proceedings of the 14th IEEE Symposium on Computer-Based Medical Systems, CBMS 2001*. IEEE; 2001:381-386.
56. Desbrun M, Meyer M, Schröder P, Barr AH. Implicit fairing of irregular meshes using diffusion and curvature flow. In: *Proceedings of the 26th Annual Conference on Computer Graphics and Interactive Techniques*. ACM Press/Addison-Wesley Publishing Co.; 1999:317-324.
57. Fan X, Hynynen K. The effect of wave reflection and refraction at soft tissue interfaces during ultrasound hyperthermia treatments. *J Acoust Soc Am*. 1992;91:1727-1736.
58. Fan X, Hynynen K. The effects of curved tissue layers on the power deposition patterns of therapeutic ultrasound beams. *Med Phys*. 1994;21:25-34.
59. Pichardo S, Hynynen K. Treatment of near-skull brain tissue with a focused device using shear-mode conversion: a numerical study. *Phys Med Biol*. 2007;52:7313-7332.
60. Jones RM, O'Reilly MA, Hynynen K. Transcranial passive acoustic mapping with hemispherical sparse arrays using CT-based skull-specific aberration corrections: a simulation study. *Phys Med Biol*. 2013;58:4981-5005.
61. Xu R, O'Reilly MA. A spine-specific phased array for transvertebral ultrasound therapy: design and simulation. *IEEE Trans Biomed Eng*. 2020;67:256-267.
62. Pennes HH. Analysis of tissue and arterial blood temperatures in the resting human forearm. *J Appl Physiol*. 1948;1:93-122.
63. Mahoney K, Fjield T, McDannold N, Clement G, Hynynen K. Comparison of modelled and observed in vivo temperature elevations induced by focused ultrasound: implications for treatment planning. *Phys Med Biol*. 2001;46:1785.
64. Hyvärinen M, Huang Y, David E, Hynynen K. Comparison of computer simulations and clinical treatment results of magnetic resonance-guided focused ultrasound surgery (MRgFUS) of uterine fibroids. *Med Phys*. 2022;49:2101-2119.
65. Daum D, Hynynen K. A 256-element ultrasonic phased array system for the treatment of large volumes of deep seated tissue. *IEEE Trans Ultrason Ferroelectr Freq Control*. 1999;46:1254-1268.
66. Clement GT, White PJ, Hynynen K. Enhanced ultrasound transmission through the human skull using shear mode conversion. *J Acoust Soc Am*. 2004;115:1356-1364.
67. Brekhovskikh LM, Godin OA. *Acoustics of Layered Media I: Plane and Quasi-Plane Waves*. Springer; 1990.
68. O'Neil HT. Theory of focusing radiators. *J Acoust Soc Am*. 1949;21:516-526.
69. Lin WL, Liauh CT, Chen YY, Liu HC, Shieh MJ. Theoretical study of temperature elevation at muscle/bone interface during ultrasound hyperthermia. *Med Phys*. 2000;27:1131-1140.
70. Scott SJ, Prakash P, Salgaonkar V, et al. Approaches for modelling interstitial ultrasound ablation of tumours within or adjacent to bone: theoretical and experimental evaluations. *Int J Hyperthermia*. 2013;29:629-642.
71. Sapareto SA, Dewey WC. Thermal dose determination in cancer therapy. *Int J Radiat Oncol Biol Phys*. 1984;10:787-800.
72. Wang J, Fujiwara O. FDTD computation of temperature rise in the human head for portable telephones. *IEEE Trans Microwave Theory Tech*. 1999;47:1528-1534.
73. Liu HL, McDannold N, Hynynen K. Focal beam distortion and treatment planning in abdominal focused ultrasound surgery. *Med Phys*. 2005;32:1270-1280.
74. Macoskey JJ, Hall TL, Sukovich JR, et al. Soft-tissue aberration correction for histotripsy. *IEEE Trans Ultrason Ferroelectr Freq Control*. 2018;65:2073-2085.
75. Yeats E, Gupta D, Xu Z, Hall TL. Effects of phase aberration on transabdominal focusing for a large aperture, low f-number histotripsy transducer. *Phys Med Biol*. 2022;67:155004.
76. Jones RM, Hynynen K. Comparison of analytical and numerical approaches for CT-based aberration correction in transcranial passive acoustic imaging. *Phys Med Biol*. 2016;61:23-36.

77. Pulkkinen A, Huang Y, Song J, Hynynen K. Simulations and measurements of transcranial low-frequency ultrasound therapy: skull-base heating and effective area of treatment. *Phys Med Biol*. 2011;56:4661-4683.
78. Delannoy B, Lasota H, Bruneel C, Torguet R, Bridoux E. The infinite planar baffles problem in acoustic radiation and its experimental verification. *J Appl Phys*. 1979;50:5189-5195.
79. Dubin AE, Patapoutian A. Nociceptors: the sensors of the pain pathway. *J Clin Invest*. 2010;120:3760-3772.
80. Bliss CI. The calculation of the dosage-mortality curve. *Ann Appl Biol*. 1935;22:134-167.
81. Yarmolenko PS, Moon EJ, Landon C, et al. Thresholds for thermal damage to normal tissues: an update. *Int J Hyperthermia*. 2011;27:320-343.
82. van Rhoon GC, Samaras T, Yarmolenko PS, Dewhirst MW, Neufeld E, Kuster N. $CEM^{\circ}_{43}C$ thermal dose thresholds: a potential guide for magnetic resonance radiofrequency exposure levels?. *Eur Radiol*. 2013;23:2215-2227.
83. Okada A, Murakami T, Mikami K, et al. A case of hepatocellular carcinoma treated by MR-guided focused ultrasound ablation with respiratory gating. *Magn Reson Med Sci*. 2006;5:167-171.
84. Aubry J-F, Pauly KB, Moonen C, et al. The road to clinical use of high-intensity focused ultrasound for liver cancer: technical and clinical consensus. *J Ther Ultrasound*. 2013;1:13.
85. Wu F, Wang ZB, Chen WZ, Bai JIN, Zhu HUI, Qiao TY. Preliminary experience using high intensity focused ultrasound for the treatment of patients with advanced stage renal malignancy. *J Urol*. 2003;170:2237-2240.
86. Wu F, Wang ZB, Zhu H, et al. Feasibility of US-guided high-intensity focused ultrasound treatment in patients with advanced pancreatic cancer: initial experience. *Radiology*. 2005;236:1034-1040.
87. de Senneville BD, Mougenot C, Moonen CTW. Real-time adaptive methods for treatment of mobile organs by MRI-controlled high-intensity focused ultrasound. *Magn Reson Med*. 2007;57:319-330.
88. Pernot M, Tanter M, Fink M. 3-D real-time motion correction in high-intensity focused ultrasound therapy. *Ultrasound Med Biol*. 2004;30:1239-1249.
89. Marquet F, Aubry JF, Pernot M, Fink M, Tanter M. Optimal transcostal high-intensity focused ultrasound with combined real-time 3D movement tracking and correction. *Phys Med Biol*. 2011;56:7061-7080.
90. Estrada S, Lu R, Conjeti S, et al.. FatSegNet: a fully automated deep learning pipeline for adipose tissue segmentation on abdominal dixon MRI. *Magn Reson Med*. 2020;83:1471-1483.
91. Chen Y, Ruan D, Xiao J, et al. Fully automated multiorgan segmentation in abdominal magnetic resonance imaging with deep neural networks. *Med Phys*. 2020;47:4971-4982.
92. Ellens NPK. *Flat, Electronically Steered $\lambda/2$-Spaced Phased Arrays for Focused Ultrasound Surgery*. PhD thesis, University of Toronto; 2015.
93. Jones RM. *Transcranial Acoustic Imaging for Guiding Cavitation-Mediated Ultrasonic Brain Therapy*. PhD thesis, University of Toronto; 2018.
94. Wang L, Wang H, Liang L, Li J, Zeng Z, Liu Y. Physics-informed neural networks for transcranial ultrasound wave propagation. *Ultrasonics*. 2023;132:107026.
95. Jaros J, Rendell AP, Treeby BE. Full-wave nonlinear ultrasound simulation on distributed clusters with applications in high-intensity focused ultrasound. *Int J High Perform Comput Appl*. 2016;30:137-155.
96. Jaros J, Vaverka F, Treeby B. Spectral domain decomposition using local fourier basis: application to ultrasound simulation on a cluster of GPUs. *Supercomput Front Innov*. 2016;3:40-55.
97. Maimbourg G, Guilbert J, Bancel T, et al. Computationally efficient transcranial ultrasonic focusing: taking advantage of the high correlation length of the human skull. *IEEE Trans Ultrason Ferroelectr Freq Control*. 2020;67:1993-2002.
98. Xu R, O'Reilly MA. Simulating transvertebral ultrasound propagation with a multi-layered ray acoustics model. *Phys Med Biol*. 2018;63:145017.
99. Seo J, Lee J. Anti-foci for focused ultrasound. *Int J Hyperthermia*. 2009;25:566-580.
100. Ebbini ES, Cain CA. Multiple-focus ultrasound phased-array pattern synthesis: optimal driving-signal distributions for hyperthermia. *IEEE Trans Ultrason Ferroelectr Freq Control*. 1989;36:540-548.

SUPPORTING INFORMATION

Additional supporting information can be found online in the Supporting Information section at the end of this article.

How to cite this article: Goudarzi S, Jones RM, Lee YHW, Hynynen K. Transducer module apodization to reduce bone heating during focused ultrasound uterine fibroid ablation with phased arrays: A numerical study. *Med Phys*. 2024;51:8670–8687.
https://doi.org/10.1002/mp.17427